Modular Design for Versatile Broadband Polarizing Metasurfaces with Freely Switching Functions

Song, Kun; Xuejian, Gong; Cao, Yunshan; Chen, Qiang; Ji, Ruonan; Liu, Yahong; Zhao, Xiaopeng; Zhou, Jiangfeng; Navarro-Cia, Miguel

DOI:
10.1002/adfm.202215105

Modular Design for Versatile Broadband Polarizing Metasurfaces with Freely Switching Functions

Kun Song, Xuejian Gong, Yunshan Cao, Qiang Chen, Ruonan Ji, Yahong Liu*, Xiaopeng Zhao, Jiangfeng Zhou, and Miguel Navarro-Cía**

K. Song, X. Gong, Y. Cao, Q. Chen, R. Ji, Y. Liu, X. Zhao
Department of Applied Physics
School of Physical Science and Technology
Northwestern Polytechnical University
Xi'an 710129, China
E-mail: songkun@nwpu.edu.cn; yhliu@nwpu.edu.cn

K. Song, R. Ji, Y. Liu
Shaanxi Basic Discipline (Liquid Physics) Research Center
School of Physical Science and Technology
Northwestern Polytechnical University
Xi'an 710129, China

J. Zhou
Department of Physics
University of South Florida
Tampa FL 33620 USA

M. Navarro-Cía
School of Physics and Astronomy & Department of Electronic, Electrical, and Systems Engineering
University of Birmingham
Birmingham B15 2TT, United Kingdom
E-mail:m.navarro-cia@bham.ac.uk

Keywords: modular design, chiral metasurfaces, versatile polarization controller,

Fabry–Pérot-like resonance, broadband

Polarization is a fundamental property of electromagnetic waves that plays a key role in many physical phenomena and applications. Schemes to manipulate it have been revisited with the emergence of metasurfaces, which have brought multi-functionalities straightforwardly. However, this has come at the expense of design complexity that relies strongly on field theory. Here, we propose an ingenious strategy of modular design to construct subwavelength multifunctional polarization control devices. Chiral metasurfaces with different handedness are first proposed and regarded as the basic modules. The versatile polarization controller can thus be obtained with the combination of different modules. Our experiments demonstrate that the well-designed polarization controller possesses reconfigurable functionality; various broadband polarization and amplitude regulation functions with high efficiency including arbitrary linear polarization rotation, asymmetric transmission effect, neutral-density-like filter, polarization beam splitter, etc., can be readily realized just by changing the cascaded modules. The physical mechanisms of the versatile polarization controller and chiral metasurface modules are both guaranteed by the Fabry–Pérot-like resonances, which are theoretically verified via the transfer matrix method. We envision that the modular concept will be of great benefit to designing compact multifunctional polarization controllers.

1. Introduction

Polarization is one of the intrinsic properties of electromagnetic (EM) waves, and the control of polarization states of EM waves plays a critical role in a wide range of modern applications, such as polarization imaging,[1-3] sensing,[4] wireless communications,[5,6] and data storage.[7] Traditional polarization control devices such as waveplates are typically based on bulky materials (e.g., birefringent crystals) and suffer from low efficiency, precluding integration in ultra-compact micro-nano optical devices. Additionally, the existence of intrinsic dispersion of nature materials also leads to a very narrow working bandwidth. Some complex designs such as Fresnel rhombs can expand the bandwidth,[8] however, their delicate structures bring

significant challenges in micro-nano fabrications. In recent years, metasurfaces, a two-dimensional version of metamaterials, provide a compact and efficient platform to tailor phases, amplitudes, and polarization states of EM waves through the abrupt phase change induced by the resonance of meta-atom.[9-12] Metasurface devices have now demonstrated extraordinary capabilities to achieve strong circular dichroism,[13-15] dynamic beamforming,[10,16] efficient polarization conversion[17-21] and vortex vector beams.[22-24]

Generally, metasurfaces with polarization conversion functions rely on specific geometry designs of sub-wavelength meta-atoms. By introducing strong anisotropy or chirality, some single-layer metasurfaces composed of gammadions,[25] fishnet structures,[26,27] plasmonic antennas,[28] nanorods,[29] L-shaped meta-atoms,[30] etc., have been proposed to realize polarization conversion. However, these metasurface-based polarization controllers are usually narrowband and display high insertion loss and angular dispersion, which are exceedingly unfavorable for practical applications. Recently, multi-layer metasurfaces dominated by Fabry–Pérot-like resonances have been demonstrated intensively to be an effective route to realize broadband and efficient polarization conversion.[31-33] However, the single functionality of the referred metasurfaces still results in a lack of application flexibility.

On the basis of active control,[34-36] structure multiplexing,[37] polarization sensitivity,[38-40] angle multiplexing,[41-43] shared-aperture,[44] and so on, multifunctional metasurfaces that can accomplish multiple polarization conversions have been proposed. For instance, Wu *et al*. designed a multifunctional wave-plate that could achieve versatile polarization regulation through the separate design of spatial unit structures.[37] Zhang *et al*. experimentally validated a multifunctional meta-polarizer of which the functionality could vary from a perfect mirror to a half-waveplate as the excitation angle changed.[45] Pitilakis *et al*. proposed a trifunctional metasurface that exhibited the functions of perfect absorption, polarization conversion, and beam splitting.[46] However, the functionalities of these metasurfaces are commonly bound to the established structure design. Once the device is fabricated, its polarization control functions are fixed, which is not favorable for adding multiple

applications in highly integrated optical systems.

In this paper, we propose an effective method for designing a versatile polarization controller inspired by the concept of modularization. Our proposed basic module is a pair of chiral enantiomer metasurfaces, which can selectively accomplish efficient and broadband linear-to-circular (LTC) or circular-to-linear (CTL) polarization conversion. By cascading different modules with properly tailored order and distance, a modular multifunctional polarization controller that can achieve more than ten different functionalities of broadband polarization control is reported. As a proof of concept, here we report in the main body of the manuscript arbitrary polarization rotation, asymmetric transmission of circularly and linearly polarized waves, circular dichroism switching, neutral-density-like filtering and polarization beam splitting. Different functionalities can be easily switched by changing the cascading order or altering the modules. As such, this modular versatile polarization controller not only expands the functionalities of polarization control devices, but also provides more manipulation convenience due to its “plug-and-play” feature. In addition, this modular design concept can be extended to terahertz frequencies, thus enabling extensive applications in a wide range of fields.

2. Design Principle and EM Properties of Chiral Metasurface Modules

Our basic module is composed of two broadband chiral enantiomeric metasurfaces. One of these metasurfaces efficiently converts linearly polarized waves to left-handed circularly polarized (LCP) waves, whereas the other efficiently transforms linearly polarized waves to right-handed circularly polarized (RCP) waves. **Figure 1**a,b illustrates the operating principle of the chiral metasurfaces. According to the different transmission responses for incident LCP and RCP waves, we term them as the left-handedness module (LHM) and right-handedness module (RHM) elements.

As shown in Figure 1c, the unit cell of the chiral metasurfaces consists of a metal-dielectric-metal tri-layer structure. The top metal pattern is an S-shaped ring surrounded by four L-shaped structures at corners, and the bottom metal layer is subwavelength metal gratings. Figure 1d shows the photograph of the fabricated LHM.

The metal patterns are made of copper with a thickness of 0.035 mm and conductivity of 5.8×10^7 S/m. The dielectric substrate is F4BM with a relative permittivity of 2.2 + 0.001**i*. The geometrical parameters of the unit cell are as follows: a = 3.5 mm, b = 2.3 mm, h_1 = 3.0 mm, l_1 = 1.0 mm, l_2 = 1.0 mm, R_1 = 3.5 mm, R_2 = 2.7 mm, w_1 = w_2 = w_3 = 0.2 mm, p = 8 mm. The subwavelength metal grating works as a linear polarizer, which allows the perpendicular linearly polarized wave to propagate through while reflecting the parallel polarized wave. The top and bottom metal layers form a subwavelength Fabry–Pérot cavity.

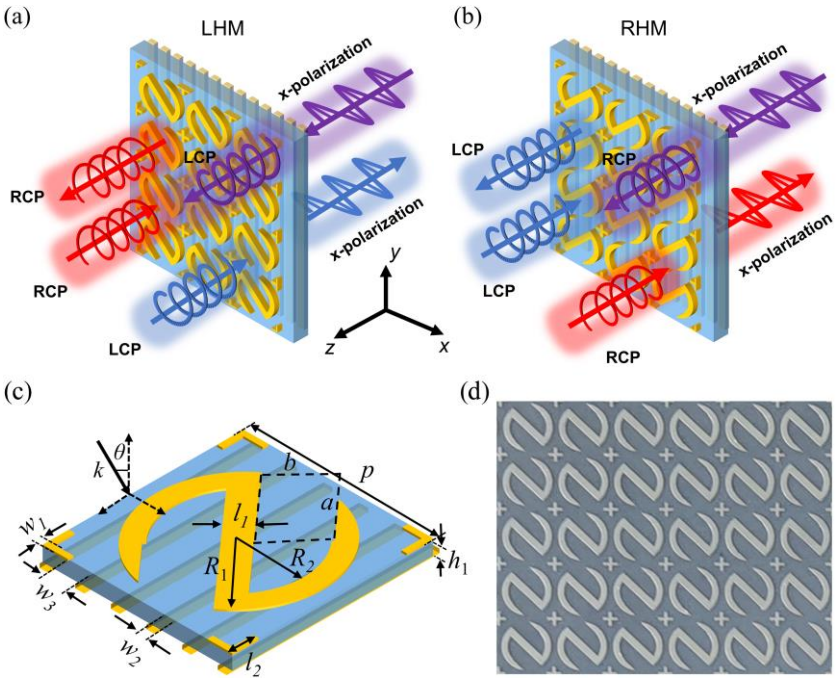

Figure 1. Operation principle of the a) LHM and b) RHM. When an *x*-polarized wave propagates along +*z* axis, the LHM (RHM) will transform it into an LCP (RCP) wave. As an LCP (RCP) wave propagates along –*z* axis, the LHM (RHM) will convert it into an *x*-polarized wave, while for the RCP (LCP) incident wave, it will be efficiently reflected by the LHM (RHM). c) Scheme of the unit cell of chiral metasurface module. d) Photograph of the LHM. The S-shaped ring is rotated clockwise by 1.5° to operate with maximum bandwidth (see Figure S2 for further insight).

The polarization conversion mechanism of our chiral metasurfaces can be explained by the interference effect of the Fabry–Pérot-like cavity. We consider an *x*-polarized plane wave passing through the metal grating incident on S-shaped ring. It

will excite dipole oscillation $\boldsymbol{p}$ along the center shaft of the S-shaped ring, which can be decomposed into two orthogonal oscillations p_x and p_y. Furthermore, multireflection caused by the Fabry–Pérot-like cavity may induce additional dipole oscillation $\boldsymbol{p'}$.[47] With a suitable length of the cavity, p_y' may enhance y component of the total transmission field, while p_x' may reduce the x component, resulting in the same magnitudes of the two orthogonal components of the total transmission field. If the phase difference between the two orthogonal transmission components satisfies the condition of $\Delta\varphi = 2n\pi \pm \pi/2$ (n is an integer), the output wave will be circularly polarized.

To confirm this interpretation, we further perform numerical simulations and theoretical calculations with transfer matrix methods (see Supporting Information).[47-49] We first consider an x-polarized wave normally incident on an LHM element from the grating side (along $+z$ direction). It is seen in **Figure 2**a that the calculated results are in good agreement with the simulation and measured ones. Between 8.8 to 12.5 GHz, the transmission coefficients of co-polarization and cross-polarization components, t_{xx} and t_{yx}, are approximately equal and both exceed 0.6 with a relative bandwidth over 34.7%. To characterize the performance of the transmitted wave, we calculate the axial ratio (AR) by the following formula:[31,50]

$$AR = 10\log\left\{\tan\left[\frac{1}{2}\sin^{-1}\frac{2\left|t_{xx}\right|\left|t_{yx}\right|\sin\Delta\varphi}{\left|t_{xx}\right|^2+\left|t_{yx}\right|^2}\right]\right\}, \quad (1)$$

where the $\Delta\varphi$ is the phase difference between co-polarization and cross-polarization components (see Figure 2b). The calculated AR in Figure 2c is less than 3 dB in the frequency region of 8.8 ~ 12.5 GHz, implying that the transmitted wave is circularly polarized. These facts mean that the chiral module can realize broadband LTC polarization conversion with high conversion efficiency $t_{xx}^2 + t_{yx}^2 > 0.95$ in 8.8 ~ 12.5 GHz. Moreover, the additional simulation results indicate that for LHM the incident x-polarized wave will be transformed into an LCP wave.

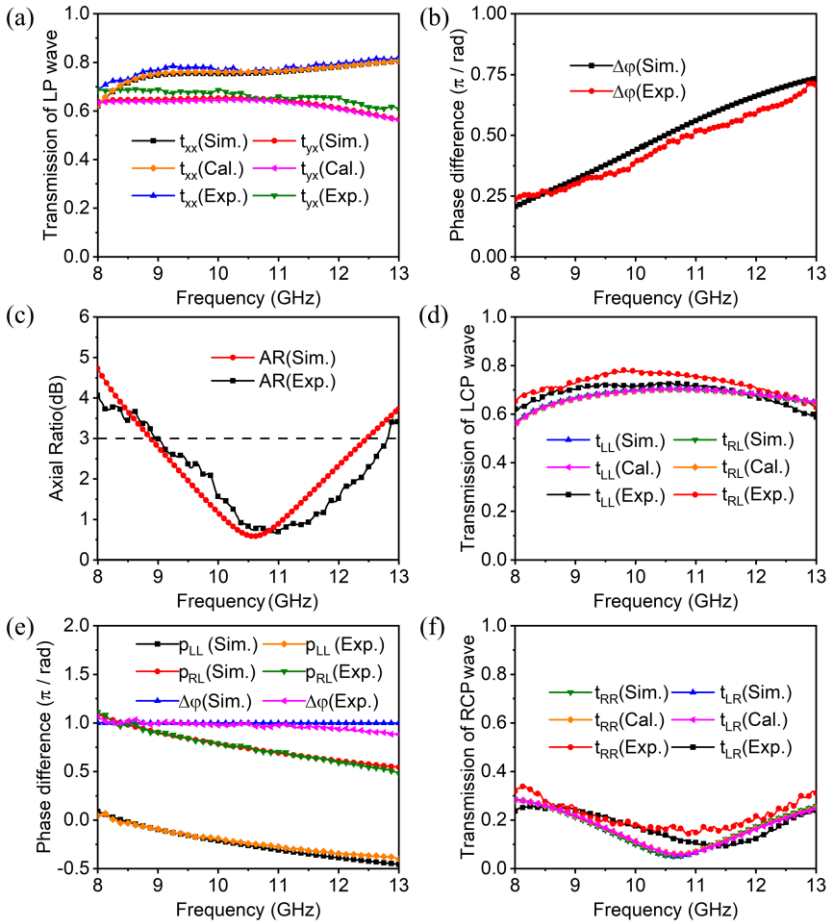

Figure 2. EM properties of the designed chiral metasurface (LHM). a) Transmission spectra and b) phase difference for the *x*-polarized wave incident from the grating side. c) The calculated AR of the transmitted wave for *x*-polarization incidence. d) Transmission spectra and e) phases for LCP waves incident from S-shaped ring side. f) Transmission spectra for RCP waves incident from S-shaped ring side.

Figure 2d presents the results of LCP waves normally incident on an LHM from the S-shaped ring side (along –*z* direction). It shows that in the frequency range of 8.8 ~ 12.5 GHz, the coefficients of cross-polarization transmission component t_{RL} are equivalent to those of co-polarization transmission component t_{LL}. Since the phase difference $\Delta\varphi$ between the two components is kept at about 180° (Figure 2e), the transmitted wave will be changed into a linearly polarized wave with the polarization direction perpendicular to the grating and the energy conversion efficiency exceeding 0.85 ($t_{LL}^2 + t_{RL}^2$). Hence, the current chiral module can also accomplish efficient CTL

polarization conversion. Besides, further numerical results reveal that these broadband and high-efficiency performances of LTC and CTL polarization conversion can be persevered over a wide range of incident angle (see Figure S3). This low angular dispersion is critical for high system performance.[51] In the case of RCP wave incidence, it can be deduced from Figure 2f that the RCP waves will be efficiently reflected as both co- and cross-polarization transmission coefficients are less than 0.3 in 8.8 ~ 12.5 GHz. Hence, our LHM element can efficiently transmit LCP waves while reflecting RCP waves, showing thus an obvious selectivity associated with chirality. Consequently, the LHM element can serve as a high-performance wide-angle and broadband polarization-dependent quarter-wave plate.

3. EM Properties of Versatile Polarization Controller Based on Chiral Modules

3.1. Freely Tunable Broadband Polarization Rotator

Polarization rotators that can tune the polarization angle to any orientation are in high demand in applications such as wireless communications and imaging. Nevertheless, most of the previous polarization rotators can rotate the polarization of EM waves only to a certain direction, giving rise to inconvenience in practical applications.[17,31] Here, we propose a novel modular broadband polarization rotator with subwavelength thickness as a solution. Our chiral metasurface module can transform circularly polarized waves into linearly polarized waves with the polarization orientation perpendicular to the grating. Consequently, for a certain circularly polarized incident wave, the polarization of the output wave can be altered to any direction if we continuously rotate the chiral module. On this basis, two LHMs presenting non-mirror symmetry in the propagation direction are assembled to form a tunable polarization rotator, as shown in **Figure 3**a,b. The polarization of the outgoing waves can be discretionarily regulated through a rotation operation acting on the second module.

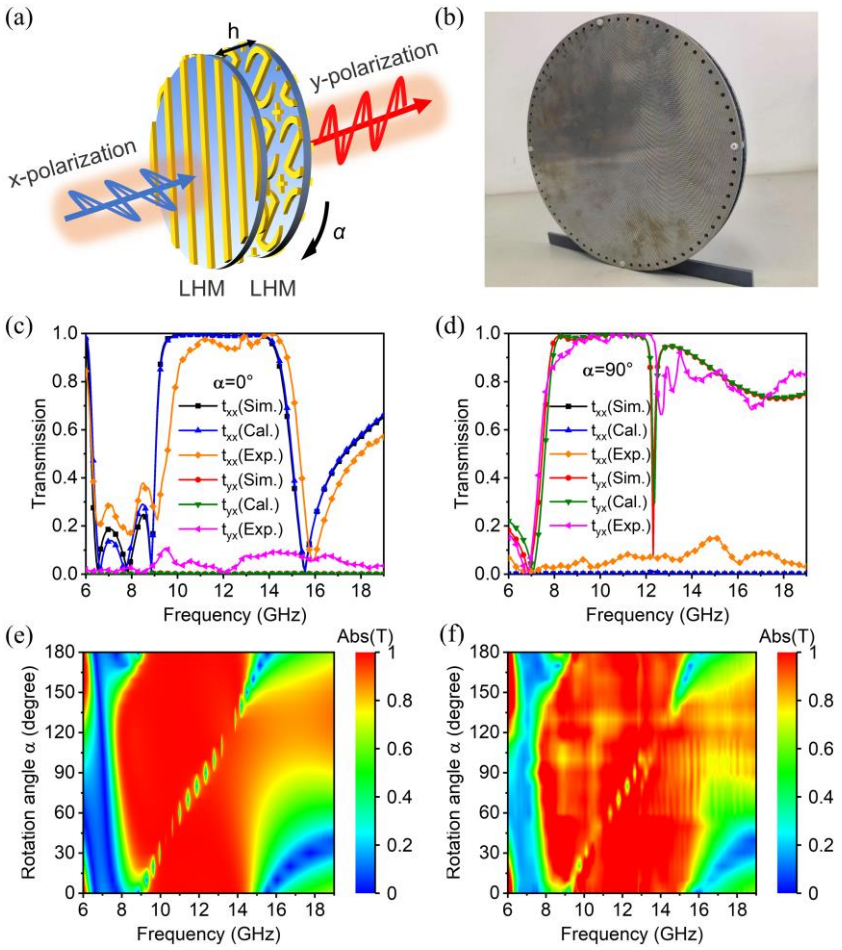

Figure 3. Numerical, theoretical and experimental results of the tunable polarization rotator. a) Schematic and b) photograph of the tunable polarization rotator. The distance between the two chiral modules is h = 4 mm. Transmission spectra for the incident x-polarized wave at c) α = 0° and d) α = 90°. e) Calculated and f) measured transmission spectra vary with the change of rotation angle α. The rotation angle step is 10°.

Figure 3c,d portrays the simulation, calculation and experimental results of the mechanically tunable polarization rotator for a normally incident x-polarized wave with the chiral module rotated by α = 0° and 90°, respectively. When the rotation angle α is 0°, the co-polarized transmission coefficients are above 0.9 over the frequency range 9.3 to 14.4 GHz while the cross-polarized coefficients are less than 0.01; this implies an efficient and broadband co-polarized output. Meanwhile, results in Figure 3d for α = 90° show that the cross-polarized transmission coefficients rise up to 0.9 over the wide 7.8 to 12.1 GHz band with the co-polarized ones no larger than 0.01; this indicates that the incident x-polarized wave will be perfectly converted

into a *y*-polarized wave, i.e., the polarization plane of output wave is rotated by 90°. Similarly, if the rotation angle α is 45°, a broadband 45° polarization rotation effect will be achieved (see Figure S4). The numerical and theoretical results plotted in Figure 3c,d show an excellent consistency, which means that there is almost no coupling effect between the two chiral modules and that the polarization rotator is governed by the Fabry–Pérot-like cavity resonance.[44] In addition, the shifts of transmission spectra between Figure 3c and Figure 3d can be attributed to the different Fabry–Pérot-like resonance effect resulting from the rotation between the two chiral modules.[33]

In order to demonstrate the arbitrary polarization rotation feature of our polarization rotator, theoretical calculations were carried out further. Owing to the C_2 symmetry of chiral modules, we just need to prove the polarization rotation properties of the polarization rotator by turning the second module from 0° to 180°. Figure 3e illustrates the theoretically calculated transmission coefficients against the rotation angle α of the second chiral module, which show excellent consistency with the experimentally measured data in Figure 3f. It is evident that the designed polarization rotator can consecutively accomplish polarization rotation with near 100% energy conversion efficiency in broad bandwidth as the rotation angle of the second chiral module changes, showing dynamical tunability. That is to say, we can obtain any desired polarization rotation simply by changing the rotation angle of the second chiral module. Thus, the well-designed device can serve as a freely tunable broadband polarization rotator with high efficiency.

3.2. Asymmetric Transmission of Circularly and Linearly Polarized Waves

Asymmetric transmission (AT)，which arises due to the different wave-structure coupling as the waves pass through the structure from opposite directions, enables many attractive applications, such as polarization rotators,[31] polarization conversion,[32,52] isolators.[53] Utilizing two chiral modules with opposite chirality, we construct a polarization control device that can realize AT effect for circularly polarized waves, as shown in **Figure 4**a.

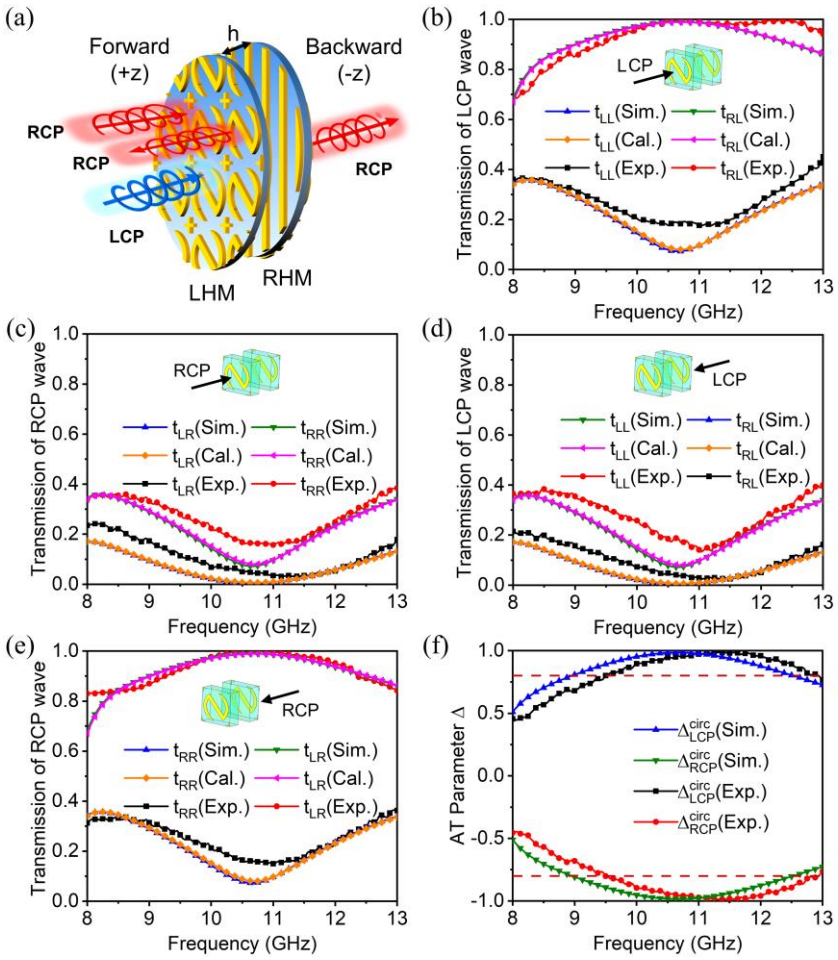

Figure 4. The results of the proposed AT device. a) Schematic of the AT device. The distance between the two chiral modules is h = 4 mm. Transmission spectra of forward propagating b) LCP and c) RCP waves. Transmission spectra of backward propagating d) LCP and e) RCP waves. f) The calculated AT parameters.

In Figure 4b,c, we present the transmission spectra of the forward propagating LCP and RCP waves (along −z axis), respectively. As illustrated by Figure 4b, for the forward LCP incident waves, the cross-polarization transmission coefficients t_{RL} are over 0.9 in 9.0 ~ 12.5 GHz while the co-polarization ones t_{LL} are not larger than 0.3. In contrast to the forward LCP incidence waves, for the forward RCP incident waves, both co- and cross-polarization transmission coefficients are less than 0.3, see Figure 4c. These results reveal that, in the case of forward incidence, the considered polarization control device enables a broadband high transmission for the LCP waves while reflecting the RCP waves efficiently. Simultaneously, the transmitted LCP waves will be transformed into RCP waves, implying a broadband and high-efficiency

cross-polarization conversion effect. Figure 4d,e shows the transmission spectra for the backward wave propagation (along +*z* axis). It is worth noting that completely inverse transmission behaviors occur for the backward propagating LCP and RCP waves compared to the results in Figure 4b,c. Thus, the combined polarization control device can realize a remarkable wideband AT effect for the circularly polarized incident waves.

To quantify the AT effect, we introduce the AT parameter Δ which is defined to characterize the difference between the transmission intensity of two opposite directions. For circularly polarized waves, it can be written in the following formulas:[32,52,53]

$$\Delta_{RCP}^{circ} = \left|t_{RR}^{f}\right|^2 + \left|t_{LR}^{f}\right|^2 - \left|t_{LR}^{b}\right|^2 - \left|t_{RR}^{b}\right|^2 = \left|t_{LR}^{f}\right|^2 - \left|t_{RL}^{f}\right|^2,$$

$$\Delta_{LCP}^{circ} = \left|t_{LL}^{f}\right|^2 + \left|t_{RL}^{f}\right|^2 - \left|t_{RL}^{b}\right|^2 - \left|t_{LL}^{b}\right|^2 = \left|t_{RL}^{f}\right|^2 - \left|t_{LR}^{f}\right|^2 = -\Delta_{RCP}^{circ}, \quad (2)$$

where the superscript '*f*' and '*b*' denote the forward and backward propagating waves, respectively; t_{LL}^{f} (t_{RR}^{f}) and t_{LL}^{b} (t_{RR}^{b}) are the co-polarized transmission coefficients of LCP (RCP) waves for the forward and backward incidence, separately; t_{RL}^{f} (t_{LR}^{f}) and t_{RL}^{b} (t_{LR}^{b}) are the corresponding cross-polarized transmission coefficients. Figure 4f depicts the AT parameter Δ of the device for the circularly polarized waves. It can be seen that in the frequency range of 9.0 ~ 12.5 GHz the values of Δ_{LCP}^{circ} are larger than 0.8, while those of Δ_{RCP}^{circ} are smaller than –0.8. This fact further demonstrates that our polarization control device allows LCP waves forward transmission and RCP waves backward transmission and blocks RCP waves forward transmission and LCP waves backward transmission, showing evident AT characteristics. Actually, in addition to AT effect for circularly polarized waves, broadband AT of linearly polarized waves can also be achieved via the combination of two chiral modules with the same chirality (Figure S5). In such a case, the device will act as a nearly perfect broadband 90° polarization rotator.

3.3. Circular Dichroism Switch and Neutral-density-like Filter

Circular dichroism has very important applications in realms such as analytical chemistry, biotechnology and imaging. Herein, we demonstrate a broadband circular dichroism switch accomplished by assembling two LHMs. The configuration of the polarization switch (α = 0°) is schematically illustrated in **Figure 5**a.

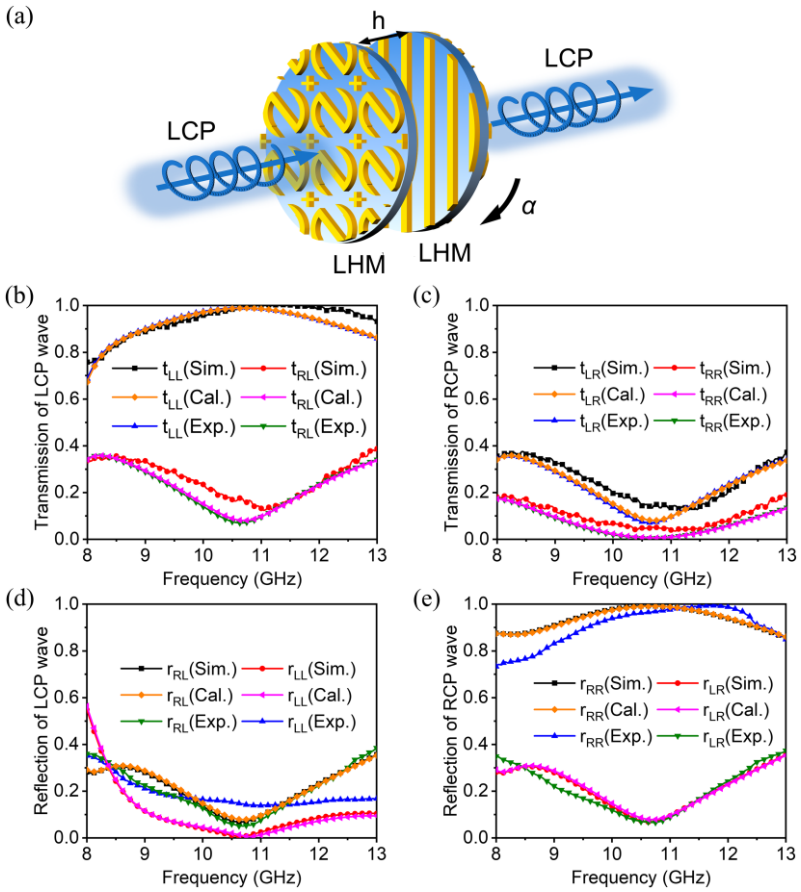

Figure 5. Numerical, theoretical and experimental results of the circular dichroism switch. a) Schematic of the circular dichroism switch. The distance between the two LHMs is h = 4 mm. The simulated, calculated and measured transmission spectra of b) LCP and c) RCP waves. The simulated, calculated and measured reflection spectra of d) LCP and e) RCP waves.

Figure 5b,c portrays the corresponding transmission spectra of our polarization switch for the LCP and RCP incident waves, respectively. It is showed in Figure 5b that the co-polarization transmission coefficients of LCP incident waves (t_{LL}) are over 0.9 from 9.0 to 12.5 GHz, while the cross-polarization ones (t_{RL}) are less than 0.3. Hence, the transmitted waves remain LCP. Meanwhile in Figure 5c, it can be found

that both co- and cross-polarization coefficients are smaller than 0.3 for the RCP incident waves, which means the RCP waves will be reflected by the polarization switch efficiently. In Figure 5d,e, we illustrate the reflection spectra for the incident LCP and RCP waves, respectively. As anticipated from the previous discussion, significant low reflection and high reflection behaviors occur for the LCP and RCP waves, respectively, further confirming the polarization-dependent transmission feature of our device. From the results described above, it is concluded that our device can operate as a high-performance wideband circular dichroism switch which enables the propagation of LCP waves. As the employed modules are both left-handedness, similar performance can also be obtained for RCP waves with two right-handedness modules.

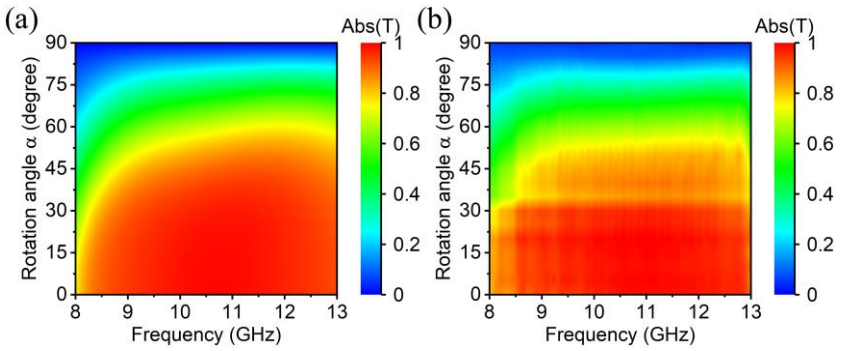

Figure 6. a) Calculation and b) experimental results of the neutral-density-like filter.

Subsequently, we execute further manipulation of the circular dichroism switch by rotating the second chiral module. **Figure 6**a,b illustrates respectively the calculated and experimental total transmission spectra of the LCP incident waves against the rotation angle α. It can be seen clearly that the total transmission of the LCP waves decreases gradually as α increases. In this case, the circular dichroism switch will alter its functionality to act as a transmission-type broadband neutral-density-like filter. When α rises up to 90°, the total transmission of the LCP waves absolutely reduces to zero. Namely, the incident LCP waves will be completely reflected by the well-designed device. At this time, our further simulations and experiments confirm that the designed device can function as a reflection-type half-wave plate or chirality preserving mirror (see Figure S6).

3.4. Polarization Beam Splitter

In **Figure 7**, we demonstrate that the functionality of polarization beam splitter can be also accomplished with two identical chiral modules. Figure 7a shows the schematic diagram of the working principle of beam splitting device. When a 45°-polarized wave is incident on the first LHM at an angle of 45°, the *y*-component will be reflected efficiently with the propagation direction perpendicular to the incident beam, while the *x*-component will firstly be converted into an LCP wave and then, after penetrating the second LHM, the LCP wave will be altered into an *x*-polarized wave further. As a result, the 45°-polarized incident wave is splitted into two orthogonal beams with propagation directions perpendicular to each other, which indicates the function as a polarization beam splitter of the proposed device.

Figure 7b plots the calculated and experimental reflection spectra of the first LHM. It is seen that the co-polarization reflectance R_{yy} is about 0.5 from 9.0 to 12.5 GHz, while the cross-polarization reflectance R_{xy} is less than 0.01. Thus, the reflected wave is a *y*-polarized wave. In Figure 7c-e, we portray the calculated and measured transmission spectra of the second LHM at α = 0°, 45°, and 90°, respectively. The experimental results agree well with the calculated data except for a slight deviation. In Figure 7c, it is obvious that, when the rotation angle α = 0°, the co-polarization transmittance T_{xx} is larger than 0.4 in a broadband frequency region of 9.6 to 11.3 GHz, while the cross-polarization transmittance is smaller than 0.01, indicating the transmitted wave is *x*-polarized. Figure 7d shows that when α = 45°, the co-polarization and cross-polarization transmittance, T_{xx} and T_{yx}, are equal to each other, and both of them are close to 0.2 from 8.7 to 11.1 GHz. Therefore, the transmitted wave is altered to be a 45°-polarization wave with a total transmittance over 0.4 in 8.7 ~ 11.1 GHz. As α is rotated to 90°, we can find in Figure 7e that the co-polarization transmittance T_{xx} is lower than 0.01 between 8.6 to 11.3 GHz, while the cross-polarization transmittance T_{yx} is larger than 0.4, implying an efficient broadband *y*-polarization transmission. Actually, the polarization of the transmitted wave of the second LHM can be freely tuned to any direction by a rotation operation, thus

providing more freedom degrees of regulation compared with the conventional polarization beam splitters. These facts confirm that the designed device can achieve the function as a polarization beam splitter in the broadband frequency range.

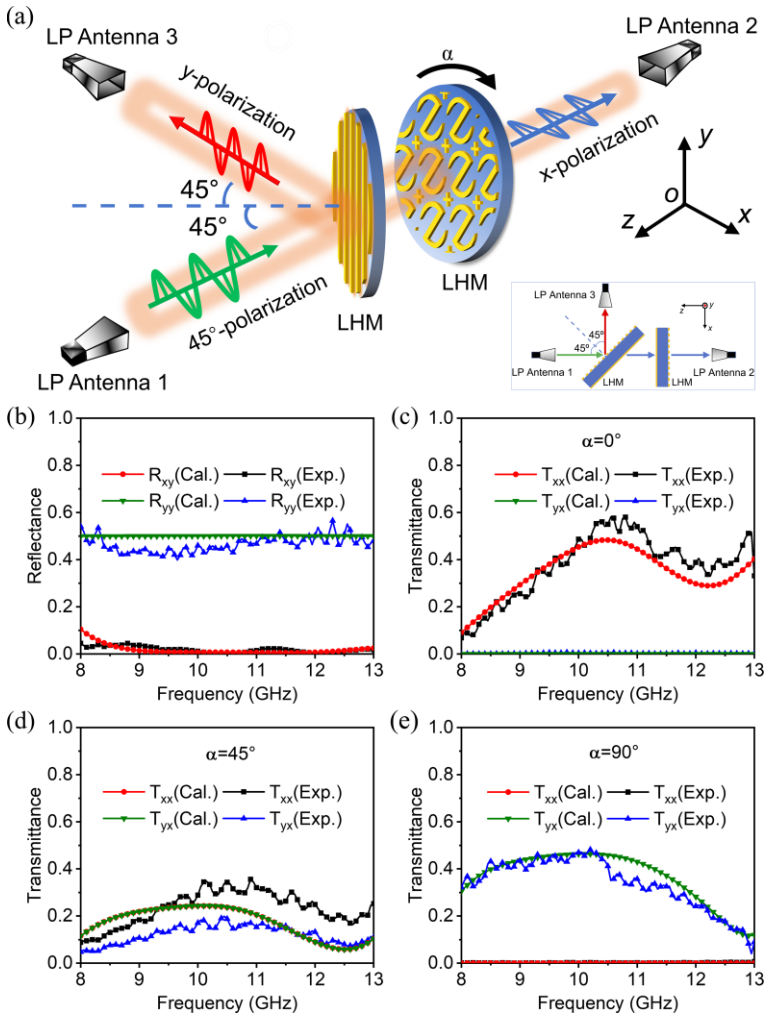

Figure 7. a) Schematic diagram of the working principle of the polarization beam splitter. The normal of the first LHM is rotated by 45° with respect to the *z*-axis, while the normal of the second LHM is parallel to the *z*-axis. The grating direction of the first LHM is along the *y*-axis. And the grating direction of the second LHM can be rotated around the *z*-axis. When the gratings of the two LHMs are paralleled to each other, the rotation angle α is defined as 0°. A 45°-polarized beam (the angle between the polarization plane and *y*-axis is 45°) is incident on the LHM at an angle of 45°. The beam emitted by antenna 1 is perpendicular to the beam received by antenna 3. The inset shows the top view of the device. b) Reflection spectra of the first LHM. Transmission spectra at c) α = 0°, (d) α = 45°, and e) α = 90° after the beam passing through the second LHM.

Finally, since our versatile polarization controller is obtained via the combination of different modules, misalignment introduced in the assembly process could potentially be a concern. Therefore, we carried out further simulations to investigate the effects of the misalignment between cascaded modules on the properties of our polarization controller. Numerical results reveal that the existence of misalignment has almost no influence on the properties of the polarization controller in different function modes (see Figure S7), which is a huge advantage for practical applications and further demonstrates the superiority of our modular polarization controller.

5. Conclusion

In this work, we have theoretically and experimentally demonstrated a modular concept to design versatile polarization controller that can be readily obtained in the same way as building blocks. Elaborate polarization-dependent chiral metasurfaces were proposed and regarded as basic modules. By combining different chiral module elements, a variety of broadband functionalities of polarization control and even amplitude regulation, for instance, freely tunable polarization rotator, asymmetric transmission effect, circular dichroism switch, neutral-density-like filter, and polarization beam splitter, have been accomplished efficiently. Meanwhile, our simulations and experiments both showed that the functions of the well-designed versatile polarization controller could be switched easily just by changing the chiral modules. The underlying physical mechanism of the versatile polarization controller has been theoretically confirmed to be the interference effect of the Fabry–Pérot-like cavity via the transfer matrix analysis. The modular design concept proposed here breaks the restriction that the functionalities of the metasurface-based polarization control devices are generally bound to the geometric structures and provides a new route to achieve multiple polarization and amplitude manipulation. Moreover, the most recent progress indicates that this modular design might also be a good candidate to realize wavefront control based on the Moiré effect.[16] Compared with the previous polarization control devices, the novel modular polarization controller possesses significant advantages of lower profile, more flexibility, lower cost, and

better maintainability, which may find important applications in wireless communication, circular dichroism spectroscopy, and highly integrated microwave or terahertz system.

Supporting Information

Supporting Information is available from the Wiley Online Library or from the author.

Acknowledgments

K. S. acknowledges support from the National Natural Science Foundation of China (Grant No. 61601375). Y. L. acknowledges support from the National Natural Science Foundation of China (Grant No. 11874301). R. J. acknowledges support from the National Natural Science Foundation of China (Grant No. 61805204). M. N.-C acknowledges support from the European Union's Horizon 2020 research and innovation program (Grant No. 777714) and the Royal Society (Grant No. IEC/NSFC/191104).

Conflict of Interest

The authors declare no conflict of interest.

References:

[1]. W. Ye, F. Zeuner, X. Li, B. Reineke, S. He, C.-W. Qiu, J. Liu, Y. Wang, S. Zhang, T. Zentgraf, *Nat. Commun.* **2016**, 7, 11930.

[2]. D. Wen, F. Yue, G. Li, G. Zheng, K. Chan, S. Chen, M. Chen, K. F. Li, P. W. H. Wong, K. W. Cheah, E. Y. B. Pun, S. Zhang, X. Chen, *Nat. Commun.* **2015**, 6, 8241.

[3]. K. Chen, Y. Feng, F. Monticone, J. Zhao, B. Zhu, T. Jiang, L. Zhang, Y. Kim, X. Ding, S. Zhang, A. Alù, C.-W. Qiu, *Adv. Mater.* **2017**, 29, 1606422.

[4]. Y. Chen, C. Zhao, Y. Zhang, C.-W. Qiu, *Nano Lett.* **2020**, 20, 8696.

[5]. W.-L. Guo, G.-M. Wang, K. Chen, H.-P. Li, Y.-Q. Zhuang, H.-X. Xu, Y. Feng, *Phys. Rev. Appl.* **2019**, 12, 014009.

[6]. L. Zhang, M. Chen, W. Tang, J. Dai, L. Miao, X. Zhou, S. Jin, Q. Cheng, T. Cui, *Nat. Electron.* **2021**, 4, 218.

[7]. P. Zijlstra, J. W. M. Chon, M. Gu, *Nature* **2009**, 459, 410.

[8]. X. Li, T.-H. Lan, C.-H. Tien, M. Gu, *Nat. Commun.* **2012**, 3, 998.

[9]. S. B. Glybovski, S. A. Tretyakov, P. A. Belov, Y. S. Kivshar, C. R. Simovski, *Phys. Rep.* **2016**, 634, 1.

[10]. N. Yu, F. Capasso, *Nat. Mater*. **2014**, 13, 139.

[11]. L. Zhang, X. Chen, S. Liu, Q. Zhang, J. Zhao, J. Dai, G. Bai, X. Wan, Q. Cheng, G. Castaldi, V. Galdi, T. Cui, *Nat. Commun.* **2018**, 9, 4334.

[12]. X. Xie, M. Pu, J. Jin, M. Xu, Y. Guo, X. Li, P. Gao, X. Ma, X. Luo, *Phys. Rev. Lett.* **2021**, 126, 183902.

[13]. Y. Zhao, M. A. Belkin, A. Alù, *Nat. Commun.* **2012**, 3, 870.

[14]. Z. Wang, L. Jing, K. Yao, Y. Yang, B. Zheng, C. M. Soukoulis, H. Chen, Y. Liu, *Adv. Mater.* **2017**, 29, 1700412.

[15]. S. Yang, Z. Liu, S. Hu, A.-Z. Jin, H. Yang, S. Zhang, J. Li, C. Gu, *Nano Lett.* **2019**, 19, 3432.

[16]. S. Liu, S. Ma, R. Shao, L. Zhang, T. Yan, Q. Ma, S. Zhang, T. Cui, *Sci. Adv.* **2022**, 8, eabo1511.

[17]. K. Song, X. Zhao, Y. Liu, Q. Fu, C. Luo, *Appl. Phys. Lett.* **2013**, 103, 101908.

[18]. S.-C. Jiang, X. Xiong, Y.-S. Hu, Y.-H. Hu, G.-B. Ma, R.-W. Peng, C. Sun, M. Wang, *Phys. Rev. X* **2014**, 4, 021026.

[19]. C.-C. Chang, Z. Zhao, D. Li, A. J. Taylor, S. Fan, H.-T. Chen, *Phys. Rev. Lett.* **2019**, 123, 237401.

[20]. Y. Li, Y. Pang, J. Wang, Q. Zheng, M. Feng, H. Ma, J. Zhang, Z. Xu, S. Qu, *Phys. Rev. Appl.* **2018**, 10, 064002.

[21]. X. You, C. Fumeaux, W. Withayachumnankul, *J. Appl. Phys.* **2022**, 131, 061101.

[22]. Y. Bao, J. Ni, C.-W. Qiu, *Adv. Mater.* **2020**, 32, 1905659.

[23]. D. Wang, F. Liu, T. Liu, S. Sun, Q. He, L. Zhou, *Light: Sci. Appl.* **2021**, 10, 67.

[24]. A. H. Dorrah, N. A. Rubin, M. Tamagnone, A. Zaidi, F. Capasso, *Nat. Commun.* **2021**, 12, 6249.

[25]. A. Papakostas, A. Potts, D. M. Bagnall, S. L. Prosvirnin, H. J. Coles, N. I. Zheludev, *Phys. Rev. Lett.* **2003**, 90, 107404.

[26]. V. A. Fedotov, P. L. Mladyonov, S. L. Prosvirnin, A. V. Rogacheva, Y. Chen, N. I. Zheludev, *Phys. Rev. Lett.* **2006**, 97, 167401.

[27]. V. Torres, N. Sánchez, D. Etayo, R. Ortuño, M. Navarro-Cía, A. Martínez, M. Beruete, *IEEE Photonics Technol. Lett.* **2014**, 26, 1679.

[28]. N. Yu, F. Aieta, P. Genevet, M. A. Kats, Z. Gaburro, F. Capasso, *Nano Lett.* **2012**, 12, 6328.

[29]. Y. Zhao, A. Alù, *Nano Lett*. **2013**, 13, 1086.

[30]. F. Xie, M. Ren, W. Wu, D. Yu, W. Cai, J. Xu, *Phys. Rev. Lett.* **2020**, 125, 237401.

[31]. L. Cong, W. Cao, X. Zhang, Z. Tian, J. Gu, R. Singh, J. Han, W. Zhang, *Appl. Phys. Lett.* **2013**, 103, 171107.

[32]. K. Song, Y. Liu, C. Luo, X. Zhao, *J. Phys. D: Appl. Phys.* **2014**, 47, 505104.

[33]. R.-H. Fan, Y. Zhou, X.-P. Ren, R.-W. Peng, S.-C. Jiang, D.-H. Xu, X. Xiong, X.-R. Huang, M. Wang, *Adv. Mater.* **2015**, 27, 1201.

[34]. L. Cong, Y. K. Srivastava, H. Zhang, X. Zhang, J. Han, R. Singh, *Light: Sci. Appl.* **2018**, 7, 28.

[35]. L. Bao, Q. Ma, R. Wu, X. Fu, J. Wu, T. Cui, *Adv. Sci.* **2021**, 8, 2100149.

[36]. X. Lv, R. T. Ako, M. Bhaskaran, S. Sriram, C. Fumeaux, W. Withayachumnankul, *IEEE Trans. Terahertz Sci. Technol.* **2022**, 12, 257.

[37]. P. C. Wu, W.-Y. Tsai, W. T. Chen, Y.-W. Huang, T.-Y. Chen, J.-W. Chen, C. Y. Liao, C. H. Chu, G. Sun, D. P. Tsai, *Nano Lett.* **2017**, 17, 445

[38]. W. Liu, Z. Li, Z. Li, H. Cheng, C. Tang, J. Li, S. Chen, J. Tian, *Adv. Mater*. **2019**, 31, 1901729.

[39]. M. Liu, W. Zhu, P. Huo, L. Feng, M. Song, C. Zhang, L. Chen, H. J. Lezec, Y. Lu, A. Agrawal, T. Xu, *Light: Sci. Appl.* **2021**, 10, 107.

[40]. C. Chen, S. Gao, W. Song, H. Li, S.-N. Zhu, T. Li, *Nano Lett.* **2021**, 21, 1815.

[41]. J. Tang, Z. Li, S. Wan, Z. Wang, C. Wan, C. Dai, Z. Li, *ACS Appl. Mater. Interfaces* **2021**, 13, 38623.

[42]. S. M. Kamali, E. Arbabi, A. Arbabi, Y. Horie, M. Faraji-Dana, A. Faraon, *Phys. Rev.*

X **2017**, 7, 041056.

[43]. Z. Shi, A. Y. Zhu, Z. Li, Y.-W. Huang, W. T. Chen, C.-W. Qiu, F. Capasso, *Sci. Adv.* **2020**, 6, eaba3367.

[44]. Q. Feng, X. Kong, M. Shan, Y. Lin, L. Li, T. Cui, *Phys. Rev. Appl.* **2022**, 17, 034017.

[45]. X. Zhang, Q. Li, F. Liu, M. Qiu, S. Sun, Q. He, L. Zhou, *Light: Sci. Appl.* **2020**, 9, 76.

[46]. A. Pitilakis, M. Seckel, A. C. Tasolamprou, F. Liu, A. Deltsidis, D. Manessis, A. Ostmann, N. V. Kantartzis, C. Liaskos, C. M. Soukoulis, S. A. Tretyakov, M. Kafesaki, O. Tsilipakos, *Phys. Rev. Appl.* **2022**, 17, 064060.

[47]. N. K. Grady, J. E. Heyes, D. R. Chowdhury, Y. Zeng, M. T. Reiten, A. K. Azad, A. J. Taylor, D. A. R. Dalvit, H.-T. Chen, *Science* **2013**, 340, 1304.

[48]. Y. Zhao, N. Engheta, A. Alù, *Metamaterials* **2011**, 5, 90.

[49]. C. Pfeiffer, A. Grbic, *Phys. Rev. Appl.* **2014**, 2, 044011.

[50]. Y. Jiang, L. Wang, J. Wang, C. N. Akwuruoha, W. Cao, *Opt. Express* **2017**, 25, 27616.

[51]. M. Navarro-Cía, V. Pacheco-Peña, S. A. Kuznetsov, M. Beruete, *Adv. Opt. Mater.* **2018**, 6, 1701312.

[52]. C. Pfeiffer, C. Zhang, V. Ray, L. J. Guo, A. Grbic, *Phys. Rev. Lett*. **2014**, 113, 023902.

[53]. C. Menzel, C. Helgert, C. Rockstuhl, E. B. Kley, A. Tünnermann, T. Pertsch, F. Lederer, *Phys. Rev. Lett*. **2010**, 104, 253902.